

*To be published in Optics Express:*

**Title:** An Asymmetric Directionally-Selective Device Based on Hyperbolic Metamaterial Slab and Photonic Band Gap  
**Authors:** Ting-Hao Zhang,BAOFEI Wan,Yu-Qi Zhao,Bingxiang Li,HaiFeng Zhang  
**Accepted:** 25 March 25  
**Posted** 27 March 25  
**DOI:** <https://doi.org/10.1364/OE.559876>

© 2025 Optica Publishing Group under the terms of the [Optica Open Access Publishing Agreement](#)

OPTICA  
PUBLISHING GROUP

# An Asymmetric Directionally-Selective Device Based on Hyperbolic Metamaterial Slab and Photonic Band Gap

TING-HAO ZHANG<sup>1</sup>, BAO-FEI WAN<sup>1</sup>, YU-QI ZHAO<sup>1</sup>, BING-XIANG LI,<sup>1,2</sup> AND HAI-FENG ZHANG<sup>1,3</sup>

<sup>1</sup>College of Electronic and Optical Engineering & College of Flexible Electronics (Future Technology), Nanjing University of Posts and Telecommunications, Nanjing 210023, China.

<sup>2</sup>bxli@njupt.edu.cn

<sup>3</sup>hanlor@163.com or hanlor@njupt.edu.cn

**Abstract:** In this paper, a theoretical research on asymmetric directional transmission-absorption device (ADTD) is proposed. Asymmetric properties based on a hyperbolic metamaterial slab (HMMS) and an angle selection function based on electromagnetic band gaps are introduced to realize the directionally-selective function. HMMS enables asymmetric properties between positive and negative incident angles. The transfer matrix method is used to calculate the transmission-absorption characteristics over a range of frequency bands in the microwave band. The ADTD consists of three basic units, unit I forms an angle selection with a right edge, unit II excites an angle selection with a left edge, and unit III creates an asymmetric transmission-absorption characteristic. The HMMS forms an absorption in the range of 16-20 GHz. The thickness of the HMMS can be adjusted to allow the asymmetric transmission-absorption bandwidth to cover a wide frequency band. HMMS implements a certain extent of angle selection, the layer-stacked metastructures enhance this effect and form a directionally-selective function. Positively incident electromagnetic waves are absorbed directionally and negatively incident electromagnetic waves pass through directionally. The excellent properties of ADTD can be used to design multifunctional optical devices.

## 1. Introduction

An absorber is a device that absorbs electromagnetic (EM) waves efficiently or attenuates them significantly [1]. By utilizing a variety of loss mechanisms, EM waves are converted into heat or other forms of energy and gradually dissipated, ultimately achieving the result of absorption [2]. EM absorbers are coated with absorbers and absorbing structures to achieve radar performance [3] and stealth performance [4]. Conventional absorbers such as ferromagnetic materials [5] are no longer able to meet current needs due to their large size and narrow operation bandwidth. EM metamaterials have exotic EM properties that do not exist in nature, and the introduction of left-handed materials in 1968 marked the birth of the concept of metamaterials [6]. In 1999, Pendry *et al.* [7] introduced the idea of artificial magnets, which consist of a periodic arrangement of sub-wavelength cellular structures with equivalent dielectric constants and magnetic permeability. EM metamaterials are designed in sub-wavelength dimensions and can be structured in special patterns to achieve extraordinary properties [8-10]. Therefore, the concept of EM metamaterial absorber has been introduced. Methods for designing the EM metamaterial absorbers have become more mature. The classical metamaterial absorbers utilize split-ring resonator [11], and metal-dielectric-metal sandwich structures [12] to achieve the absorbing effect, which have smaller sizes and better absorbing performance. However, few studies have been conducted on the design of directionally-selective functions.

As EM metamaterials and their related theories continue to mature, novel metamaterial designs continue to emerge [13-15]. In recent years, hyperbolic metamaterials (HMMs) have received much attention [16]. HMM is a unit with strong anisotropy. Its iso-frequency surface is an open hyperboloid, unlike the iso-frequency surface of ordinary medium which is a closed

spherical or ellipsoidal surface. HMM has excellent modulation characteristics for near-field EM waves. There has been a great deal of research on HMMs, including surface plasmon [17], negative refraction [18], etc. HMMs are mainly classified into electric HMMs and magnetic ones, which correspond to the three-dimensional matrices of the dielectric tensor and the magnetic permeability tensor. Then the problem of anomalous transport about HMM is much more than that. In this paper, the unit of HMM slab (HMMS) is proposed. HMMS is a thin film structure with HMM properties that has a dielectric tensor similar to that of uniaxial crystals. Since the size of HMMS is small enough, it can be brought into the transfer matrix method (TMM) for calculation. It plays a vital role in realizing the transmission-absorption and angular domain properties of EM waves. The theoretical proposal of HMMS brings new ideas for the modulation of EM waves.

The study of the fundamental properties of EM waves has become increasingly sophisticated, including the study of frequency and polarization [19-21]. Research on directional control of planar EM waves has developed rapidly [22, 23]. The directional control of EM waves can be defined as angle selection. In 2014, Shen *et al.* [24] pioneered the study of angle selection by building a photonic crystals stack structure using Brewster's angle to realize angle selection of transverse magnetic (TM) waves and verified it in experiments. Since then, a large amount of work on angle selection has spilled out. In 2016, Iizuka *et al.* [25] designed a polarization-independent angle edge state using the edge states of photonic band gap (PBG) and its anomalous dispersion properties in the region of extremely small wave vectors. The angle selection formed by PBG was extremely excellent. In 2018, Qu *et al.* [26] introduced a half-wave plate structure, and angle selection was also formed for TE (transverse electric) waves using the Brewster angle, but the transmission performance was inadequate. In 2021, Xu *et al.* [27] synthesized a gradient epsilon-near-zero (ENZ) material by stacking multiple ENZ materials to achieve broadband angle selection. Liu *et al.* [28] used ENZ materials to achieve non-inverse thermal radiation. The common feature of these angle-selective methods is the ability to excite angle edge states. When two angle edge states exist simultaneously, the transmission window can be spliced to form multiple channels [29]. Angle selection has a very wide range of applications in the fields of sensing systems [30], signal processing [31], information communication [32], solar energy conversion [33], and antenna modulation [34]. However, the directional modulation of asymmetric EM waves is still in the initial state, and the selectivity of the asymmetric directional modulation achieved so far is poor.

In this paper, an asymmetric directional transmission-absorption device (ADTD) is proposed. The absorption difference between positive and negative angles ( $+\theta_s$  and  $-\theta_s$ ) formed by the HMMS and the transmission window formed by stitching the PBG are simultaneously introduced to achieve the function of directional selection. The HMMS consists of a solid-state plasma stacked with an isotropic dielectric, and the PBG is fully excited by the isotropic dielectric. The selective symmetric angle transmission window formed by the PBG and the asymmetric absorption window obtained by the HMMS create a directional absorption effect at  $+\theta_s$ . Similarly, the PBG and the asymmetric transmission window formed by the HMMS create a directional transmission effect at  $-\theta_s$ . This method has potential value in the optics and physics field and may be applied to multifunctional optical device design, privacy protection, and other fields. In addition, the research in this paper is purely theoretical, the rationality of the theory is thoroughly verified.

## 2. Theory and configuration

The proposed ADTD is shown in Fig.1 and the three units are unit I Metastructure<sub>1</sub> (MS<sub>1</sub>), unit II (MS<sub>2</sub>), and unit III (HMMS). Where MS<sub>1</sub> excites the left edge, MS<sub>2</sub> excites the right edge, and the HMMS realizes the absorption function. MS<sub>1</sub> is formed by stacking media AB in layers, MS<sub>2</sub> is formed by stacking dielectrics C and D, and the HMMS is formed by stacking media E, and F is tilted at 18° in +x direction. A and A<sub>1</sub> indicate different thicknesses of layers corresponding to the same medium in the overall structure. The specific structure of

MS<sub>1</sub> is A<sub>1</sub>B<sub>1</sub>AB<sub>1</sub>(AB)<sup>10</sup>AB<sub>1</sub>A<sub>1</sub>, where the (AB)<sup>10</sup> in the middle is the main structure, the structures on both sides are the anti-reflective layers (AL), the AL consists of the same medium as that used for the main structure. The refractive indexes are  $n_A=n_{A1}=3.28$ ,  $n_B=n_{B1}=1.8$ , the thicknesses are  $d_A=5.5$  mm,  $d_{A1}=2.8$  mm,  $d_B=2.3$  mm,  $d_{B1}=2.1$  mm. MS<sub>2</sub> can be represented as C<sub>1</sub>(D<sub>1</sub>C)<sup>3</sup>D<sub>1</sub>(CD)<sup>12</sup>(CD<sub>1</sub>)<sup>3</sup>C<sub>1</sub>, similar to MS<sub>1</sub>, it also consists of the main structure (CD)<sup>12</sup> and AL. Where  $n_C=n_{C1}=2.45$ ,  $n_D=n_{D1}=1.49$ ,  $d_C=5.9$  mm,  $d_{C1}=3$  mm,  $d_D=2.3$  mm,  $d_{D1}=2.5$  mm. The HMMS consists of a solid-state plasma [36] and a dielectric E, where  $n_E=2$ , the thickness of the solid-state plasma is  $d_p=0.1$  mm, and the thickness of E is  $d_E=0.4$  mm, the thickness of a period in HMMS is  $d=d_E+d_p$ . In the propagation direction +z, the thickness of the HMMS is  $W=5$  mm. Among them, dielectrics A, B, C, D, and E are all lossless isotropic dielectrics, and in photonic crystals research, only the dielectric refractive indices can be given to make the expression more concise. Of course, these dielectric refractive indices can be found in nature or obtained by synthetic methods, and are not the focus in this paper.

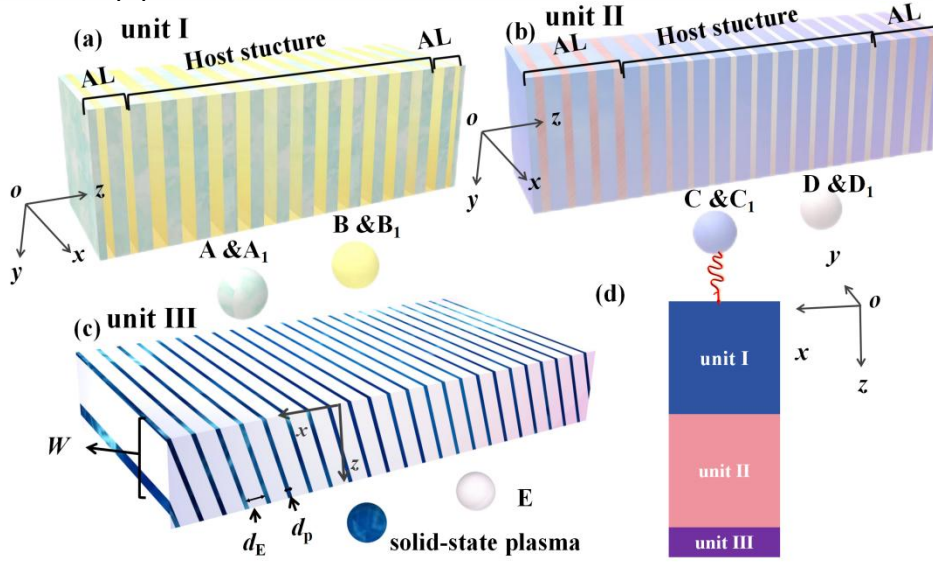


Fig.1. Schematic diagram of the structure units of the ADTD, (a) MS<sub>1</sub>, (b) MS<sub>2</sub>, (c) HMMS, and (d) the splicing method of ADTD.

Due to the hyperbolic nature of HMMS, it is equated to a uniaxial crystal in the calculation of HMMS. The dielectric arrangement of the HMMS is exhibited in Fig.2 (a), and the thickness of each period is  $d=0.5$  mm. The dimensions of the periodic structural units in the HMMS are much smaller than the wavelength of the incident EM waves, which can be calculated by the equivalent dielectric theory [35]. As shown in Fig.2 (a), the given HMMS structure is in a tilted arrangement.

The dielectric constant of solid-state plasma can be expressed by the following equation [36]:

$$\varepsilon_m = 12.4 - \frac{\omega_p^2}{\omega(\omega + i\gamma)} \quad (1)$$

where  $\omega_p$  represents the plasma frequency,  $\omega_p=(e^2N_e/\varepsilon_0m)^{1/2}$ ,  $\omega=2\pi f$ ,  $\gamma=0.01\omega_p$  is the damping constant of the loss, where  $N_e=1.2 \times 10^{20} \text{ m}^{-3}$ ,  $\varepsilon_0=8.854 \times 10^{-12} \text{ F/m}$ ,  $e=1.6 \times 10^{-19} \text{ C}$ ,  $m=9.11 \times 10^{-31} \text{ Kg}$  [36]. The high-frequency dielectric constant of the solid-state plasma is 12.4, which is directly expressed as a numerical value in (1). When the wavelength of the EM wave is much

larger than  $d$ , the composite permittivity consisting of the solid-state plasma and the medium E can be found by Maxwell Garnett equivalent medium theory [35], and the full tensor form of the composite medium is [35]:

$$\tilde{\boldsymbol{\epsilon}} = \begin{pmatrix} \epsilon_{xx} & 0 & 0 \\ 0 & \epsilon_{yy} & 0 \\ 0 & 0 & \epsilon_{zz} \end{pmatrix}. \quad (2)$$

Where

$$\epsilon_{xx} = \frac{\epsilon_e \epsilon_m}{\epsilon_e f_m + \epsilon_m f_e}. \quad (3)$$

$$\epsilon_{yy} = \epsilon_{zz} = \epsilon_m f_m + \epsilon_e f_e. \quad (4)$$

where  $\epsilon_e$  denotes the dielectric constant of the medium E of magnitude  $n_{\mathbf{E}}^2$ ,  $f_m$  presents the volume fraction of solid-state plasma in a layer of composite medium, and  $f_e$  is the volume fraction of the dielectric E therein. To obtain the desired constructed HMMS, the original HMMS is rotated in the  $+x$ -direction along the  $xoz$ -plane by  $\varphi=18^\circ$ , as shown in Fig.1 (c). For HMMS with a change in the main optical axis, the angular change basic tensor is introduced for calculation and the changed tensor form can be expressed as [37]:

$$\tilde{\boldsymbol{\epsilon}} = \begin{pmatrix} \epsilon_{xx} & 0 & \epsilon_{xz} \\ 0 & \epsilon_{yy} & 0 \\ \epsilon_{zx} & 0 & \epsilon_{zz} \end{pmatrix}. \quad (5)$$

where

$$\epsilon_{xx} = \epsilon_{xx} \cos^2 \varphi + \epsilon_{yy} \sin^2 \varphi. \quad (6)$$

$$\epsilon_{xz} = \epsilon_{zx} = (\epsilon_{yy} - \epsilon_{xx}) \sin \varphi \cos \varphi. \quad (7)$$

$$\epsilon_{zz} = \epsilon_{xx} \sin^2 \varphi + \epsilon_{yy} \cos^2 \varphi. \quad (8)$$

When EM waves are incident into the medium under the TM mode, the EM field within the medium is formed when the  $+z$  direction and  $-z$  direction EM waves are superimposed. For isotropic dielectrics, the wave vectors in both directions are equal in magnitude. For a composite medium such as a HMMS, the wave vectors in both directions are no longer equal in size due to the change in the optical axis. The corresponding conventional transmission matrix needs to be adjusted in response, and source-free Maxwell equations [38] are used to solve it:

$$\nabla \cdot \mathbf{D} = \rho_0. \quad (9)$$

$$\nabla \times \mathbf{E} = -i\omega \mathbf{B}. \quad (10)$$

$$\nabla \cdot \mathbf{B} = 0. \quad (11)$$

$$\nabla \times \mathbf{H} = \mathbf{J} + i\omega \mathbf{D}. \quad (12)$$

For TM waves, the magnetic field has a component only in the  $y$ -direction, and the electric field can be decomposed into the  $x$  and  $z$  directions; the magnetic field in an HMMS can be expressed as:

$$H_y = H_y^+ \hat{y} + H_y^- \hat{y} = H_{y0}^+ e^{i(k_z^+ z + k_x x - \omega t)} \hat{y} + H_{y0}^- e^{i(k_z^- z + k_x x - \omega t)} \hat{y}. \quad (13)$$

where  $k_z^+$  and  $k_z^-$  indicate the components of the  $z$ -direction wavevector along the  $+z$  and  $-z$  axes, which can be obtained by bringing the resulting magnetic field into Maxwell equations:

$$\nabla \times \mathbf{H} = \begin{vmatrix} \hat{x} & \hat{y} & \hat{z} \\ \frac{\partial}{\partial x} & \frac{\partial}{\partial y} & \frac{\partial}{\partial z} \\ 0 & H_y & 0 \end{vmatrix} = (-ik_z^+ H_y^+ - ik_z^- H_y^-) \hat{x} + ik_x (H_y^+ + H_y^-) \hat{z}. \quad (14)$$

From the relationship between the electric flux density and the electric field vector  $\mathbf{D} = \epsilon_0 \epsilon \mathbf{E}$  and (6)-(8):

$$\begin{pmatrix} D_x \\ 0 \\ D_z \end{pmatrix} = \epsilon_0 \begin{pmatrix} \epsilon_{xx} & 0 & \epsilon_{xz} \\ 0 & \epsilon_{yy} & 0 \\ \epsilon_{zx} & 0 & \epsilon_{zz} \end{pmatrix} \begin{pmatrix} E_x \\ 0 \\ E_z \end{pmatrix}. \quad (15)$$

$$\nabla \times \mathbf{H} = -i\omega \epsilon_0 (\epsilon_{xx} E_x + \epsilon_{xz} E_z) \hat{x} - i\omega \epsilon_0 (\epsilon_{zx} E_x + \epsilon_{zz} E_z) \hat{z}. \quad (16)$$

From (12),

$$\begin{cases} k_z^+ H_y^+ + k_z^- H_y^- = \omega \epsilon_0 (\epsilon_{xx} E_x + \epsilon_{xz} E_z) \\ k_x (H_y^+ + H_y^-) = \omega \epsilon_0 (\epsilon_{zx} E_x + \epsilon_{zz} E_z) \end{cases}. \quad (17)$$

So,  $E_x$  can be presented as:

$$E_x = \frac{\epsilon_{zz} k_z^+ + \epsilon_{xz} k_x}{\omega \epsilon_0 (\epsilon_{xx} \epsilon_{zz} - \epsilon_{xz}^2)} H_y^+ + \frac{\epsilon_{zz} k_z^- + \epsilon_{xz} k_x}{\omega \epsilon_0 (\epsilon_{xx} \epsilon_{zz} - \epsilon_{xz}^2)} H_y^-. \quad (18)$$

The wave vector  $k_x$  in the  $+x$ -direction is always constant, and when solving for  $k_z$ , it follows from (6):

$$\frac{\partial E_x}{\partial z} - \frac{\partial E_z}{\partial x} = i\omega \mu_0 \mu_r H_y^+. \quad (19)$$

Carrying (17) and (18) into (19) for generalization yields:

$$\epsilon_{zz} k_z^2 + (\epsilon_{xz} k_x + k_x \epsilon_{zx}) + \epsilon_{xx} k_x^2 = k_0^2 (\epsilon_{xx} \epsilon_{zz} - \epsilon_{xz}^2). \quad (20)$$

The  $k_z$  is solved to have two solutions, which are:

$$\begin{cases} k_z^1 = \left[ -\varepsilon_{xz} k_x + \sqrt{(\varepsilon_{xz}^2 - \varepsilon_{zz} \varepsilon_{xx}) (k_x^2 - k_0^2 \varepsilon_{zz})} \right] / \varepsilon_{zz} \\ k_z^2 = \left[ -\varepsilon_{xz} k_x - \sqrt{(\varepsilon_{xz}^2 - \varepsilon_{zz} \varepsilon_{xx}) (k_x^2 - k_0^2 \varepsilon_{zz})} \right] / \varepsilon_{zz} \end{cases} \quad (21)$$

These two solutions for  $k_z$  correspond to two opposite directions of propagating EM waves in the HMMS. During the transport of EM waves, EM waves traveling in different directions in the  $z$ -direction project different electric field vectors in the solid-state plasma layer, creating different interactions. The dispersion properties of HMMS are plotted in Fig.2 (b).  $k_z^0$  corresponds to the curve representing the dispersion curve of a normal medium as a closed circle.  $k_z^1$  and  $k_z^2$  represent the real part of the two wave vectors with opposite directions in the  $z$ -direction in HMMS. The two wave vectors of the  $z$  component in the HMMS in the iso-frequency lines show hyperbolic curves, which indicates the hyperbolic relation is satisfied.

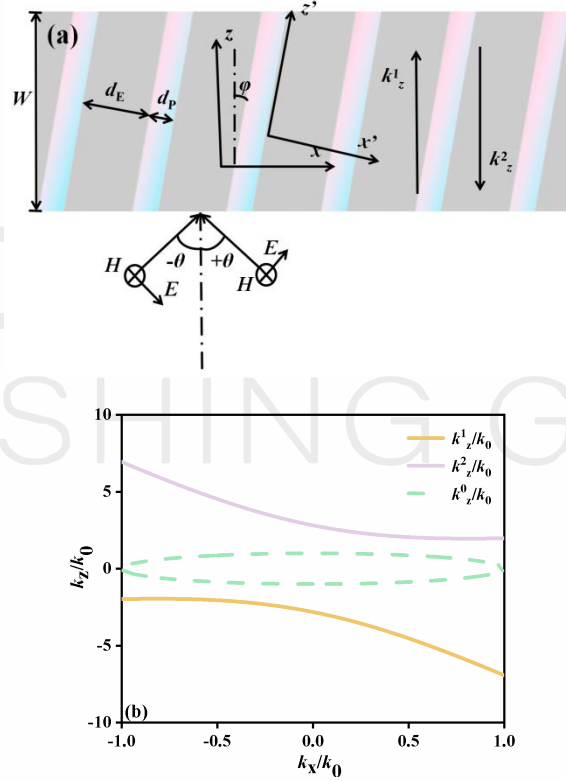


Fig. 2. (a) Schematic diagram of one-dimensional structure arrangement of HMMS, and (b) dispersion characteristics of HMMS and common media.

In the calculation of metamaterials using the TMM, the transverse wave impedance is defined as  $Z$ , which can be expressed by the following equation:

$$Z = - \frac{(k_x^2 - k_0^2 \varepsilon_{zz})}{\omega \varepsilon_0 (\varepsilon_{xz}^2 - \varepsilon_{xx} \varepsilon_{zz})}. \quad (22)$$

According to the boundary conditions, it is known that the EM field is continuous at the interface of layers  $i$  and  $j$ .  $E_x$  can be expressed as by  $Z$ :

$$E_x = ZH_y^+ - ZH_y^-. \quad (23)$$

$$\begin{aligned}
H_{y_i}^+ + H_{y_i}^- &= H_{y_j}^+ + H_{y_j}^- \\
Z_i H_{y_i}^+ - Z_i H_{y_i}^- &= Z_j H_{y_j}^+ - Z_j H_{y_j}^-.
\end{aligned} \tag{24}$$

Written in matrix form, equation (24) can be expressed as:

$$\begin{bmatrix} 1 & 1 \\ Z_i & -Z_i \end{bmatrix} \begin{bmatrix} H_{y_i}^+ \\ H_{y_i}^- \end{bmatrix} = \begin{bmatrix} 1 & 1 \\ Z_j & -Z_j \end{bmatrix} \begin{bmatrix} H_{y_j}^+ \\ H_{y_j}^- \end{bmatrix}. \tag{25}$$

The transfer matrix at the interface is defined [39]:

$$\mathbf{T} = \begin{bmatrix} 1 & 1 \\ Z & -Z \end{bmatrix}. \tag{26}$$

Equation (26) can take the form of:

$$\mathbf{T}_i \begin{bmatrix} H_{y_i}^+ \\ H_{y_i}^- \end{bmatrix} = \mathbf{T}_j \begin{bmatrix} H_{y_j}^+ \\ H_{y_j}^- \end{bmatrix}. \tag{27}$$

The phase transfer matrix of EM waves in a HMMS is:

$$\mathbf{P} = \begin{bmatrix} e^{-ik^2 w} & 0 \\ 0 & e^{-ik^1 w} \end{bmatrix}. \tag{28}$$

The transfer matrix at the air-medium interface is:

$$\mathbf{T}_1 = \begin{bmatrix} 1 & 1 \\ \sqrt{\frac{\mu_0}{\varepsilon_0}} \cos \theta & -\sqrt{\frac{\mu_0}{\varepsilon_0}} \cos \theta \end{bmatrix}. \tag{29}$$

For the HMMS, the total transfer matrix can be written as:

$$\mathbf{M} = \mathbf{T}_1^{-1} \mathbf{T}_2 \mathbf{P} \mathbf{T}_2^{-1} \mathbf{T}_1. \tag{30}$$

$H_{in}$ ,  $H_{out}$ , and  $H_r$  refer to the magnetic fields of incident, outgoing, and reflected EM waves, respectively, the following relations are satisfied:

$$\begin{bmatrix} H_{in} \\ H_r \end{bmatrix} = \mathbf{M} \begin{bmatrix} H_{out} \\ 0 \end{bmatrix} = \begin{bmatrix} M_{11} & M_{12} \\ M_{21} & M_{22} \end{bmatrix} \begin{bmatrix} H_{out} \\ 0 \end{bmatrix}. \tag{31}$$

Transmissivity  $Tr$ , reflectivity  $R$ , and absorptivity  $A$  can be derived from the following equation:

$$Tr = \left| \frac{H_{out}}{H_{in}} \right|^2 = \left| \frac{1}{M_{11}} \right|^2$$

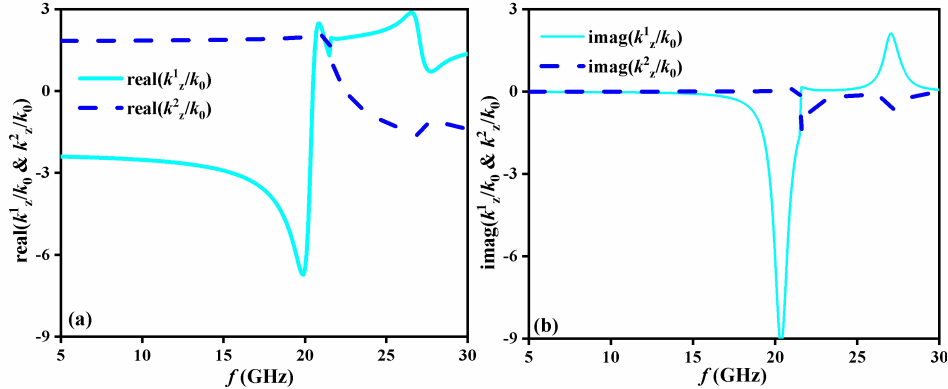
$$R = \left| \frac{H_r}{H_{in}} \right|^2 = \left| \frac{M_{21}}{M_{11}} \right|^2 \quad (32)$$

$$A = 1 - Tr - R.$$

The directional selection function is formed by the PBG of MS<sub>1</sub> and MS<sub>2</sub>, which only contains isotropic dielectrics. When performing calculations for isotropic dielectrics, only the generalized transfer matrix of the HMMS needs to be properly degenerated, which just change the dielectric tensor form of HMMS to an isotropic dielectric form, which only has numerical values on the main diagonal and all three values are completely equal. The specific calculation method for isotropic dielectrics can be found in Ref.39, no further detailed discussion will be provided here.

### 3. Discussion and analysis

When the incident EM wave enters the surface of a medium in the TM mode, if  $\theta$  reaches a specific value, the wave will pass through completely without reflection. This phenomenon is known as the Brewster effect [40]. For the classical Brewster angle, the ratio of the refractive indices is equal to the ratio of the tangents of the  $\theta$ s, which is shown in Fig.1 for EM waves incident along  $-\theta$ s. As given in Fig.1. EM waves incident along  $+\theta$ s, where the transmitted EM wave is absorbed in the lossy medium. This effect is defined as the anomalous Brewster effect. For an incident EM wave at  $+\theta$ , the equivalent permittivity of the HMMS can be expressed in terms of  $\varepsilon_{yy}$ , which is derived from arctan to obtain the anomalous Brewster angle as  $+56.7^\circ$  [40]. In Figs.3 (a), (b), and (c), the HMMS demonstrates unrivaled absorption properties. It is worth noting that the scale of the HMMS is much more minor than the corresponding wavelength scale, and the loss of used solid-state plasma is related to  $\gamma$ . The abnormal transmission behavior caused is due to the strong resonance effect between the solid-state plasma and the EM waves from  $+\theta$ s, resulting in absorption, while no resonance occurs for the ones incident from  $-\theta$ s. As shown in Fig.3 (a), the normalization coefficients of the two waves along the  $+z$  and  $-z$  directions are reacted, and Fig.3 (b) reacts to the variation of the imaginary part of the two waves. It can be seen that when the imaginary part of the wave vector is not at 0, which corresponds to the position where the absorption occurs, the jump of the imaginary part of the wave vector on the positive and negative scales corresponds to the jump of the absorption at the same frequency point. The amplitude of the imaginary part is maximized around 20 GHz in Fig.3 (c), which corresponds to the point in Fig.3 (a) where the absorption is highest, and high absorption ( $A > 0.9$ ) is achieved when the normalized wavevector reaches a designated value.



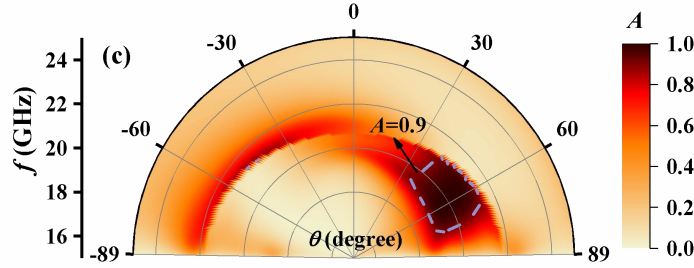


Fig.3. (a) Normalized real part of two opposite plane waves in HMMS, (b) normalized imaginary part of two opposite plane waves in HMMS, and (c) absorption of HMMS for different  $\theta$ s and frequencies of incident EM waves.

In Fig.4 the impedance matching characteristics and the anomalous Brewster effect of HMMS are represented. In Fig.4 (a),  $f=19.5$  GHz is chosen for the discussion, and impedance matching in the angular domain is demonstrated. From Fig.4(a), it can be seen that the impedance matching characteristics are exactly the same for  $+\theta$ s and  $-\theta$ s. Near-perfect impedance matching conditions are achieved when  $\theta$  is around  $\pm 56.7^\circ$ . The absorption and transmission properties of HMMS are demonstrated in Fig.4 (b). The phenomenon of perfect transmission occurs when the EM waves incident at the Brewster angle, and complete absorption occurs when they incident at the anomalous Brewster angle. When  $\theta$  deviates from these two angles, the reflection is no longer suppressed, leading to a decrease in absorption and transmission. Absorption and transmission show an approximate symmetry at  $+\theta$ s and  $-\theta$ s and supply a new idea for the design of directionally-selective devices due to the increasing selectivity of the reflection.

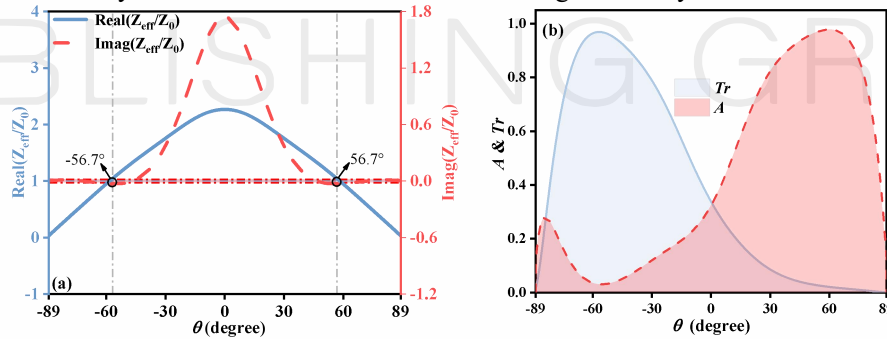


Fig.4. (a) Wave impedance characteristics corresponding to different  $\theta$ s at  $f=19.5$  GHz in HMMS, and (b) Asymmetric absorption-transmission properties of HMMS in the angular domain.

To further optimize the selectivity on the angular domain, PBG is introduced.  $MS_1$  and  $MS_2$  excite two angle edge states, respectively, and both consist of a main body structure and ALs. Since dielectrics A, B, C and D are isotropic lossless dielectrics without absorption effects, the positions of the PBGs excited by these dielectrics represent the region of  $R=1$ . The angle edge states excited by  $MS_1$  and  $MS_2$  are due to the PBGs therein. In Figs.5 (a) and (b), specific variations of the PBGs are shown. As shown in Fig.5 (a), the left edge of the PBG blueshifted as  $\theta$  increases. The corresponding frequency window (FW, the position of spectral jumps in the frequency domain) moves from 19.2 GHz to 20 GHz when  $\theta$  increases from  $30^\circ$  to  $50^\circ$ . The corresponding FW maintains a high stability when  $\theta$  is shifted. This excellent characteristic can be demonstrated in the angular domain. The PBG at the right edge is shown in Fig.5 (b), where the corresponding FW moves to high frequencies when  $\theta$  increases. When  $\theta$  increases from  $55^\circ$  to  $65^\circ$ , the corresponding frequency of the FW moves from 19.2 GHz to 19.6 GHz.

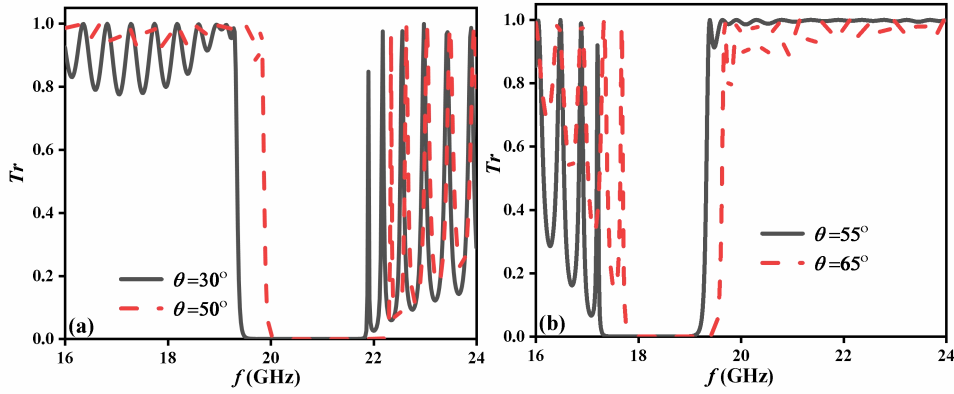
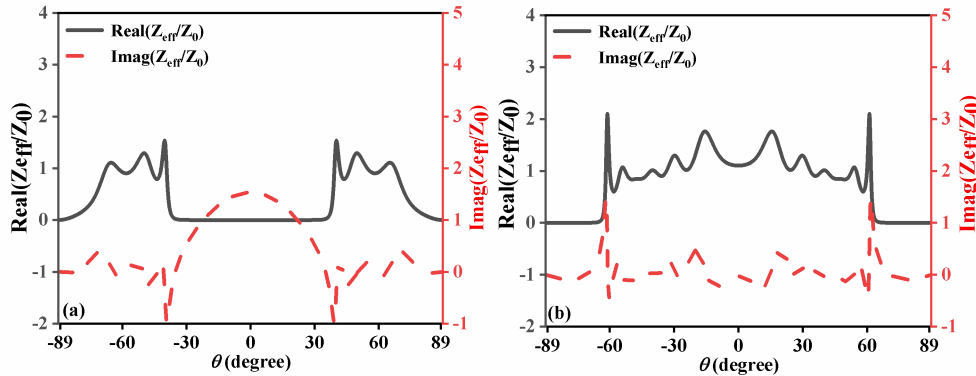


Fig.5. (a) PBG of MS<sub>1</sub> at  $\theta=30^\circ$  and  $\theta=50^\circ$  corresponding positions, and (b) PBGs of MS<sub>2</sub> are at the positions of  $\theta=55^\circ$  and  $\theta=65^\circ$ , respectively.

In the process of designing angle selection using PBGs, AL [41] is introduced to improve the angle-selective performance. Figs.6 (a) and (b) represent the planar structures of MS<sub>1</sub> and MS<sub>2</sub>, with the same middle laminated stack AB and CD being the main structure and the structures on either side being the AL. Generally, the AL has the same material composition as the main structure. There will be a difference in thickness. An example is the arrangement of MS<sub>1</sub> reflected in Fig.1 (a) and MS<sub>2</sub> reflected in Fig.1 (b). Both of these structures are in similar arrangements to that adopted by Iizuka [25]. Fig.6 (c) reflects the enhancement of the angle edge state of MS<sub>1</sub> by the introduction of the AL. The situation without AL is also plotted, the lowest point of the transmission is at  $Tr=0.65$ . After the introduction of the AL, the lowest point of the transmission is maintained at the level of  $Tr>0.9$  all along. The effect of the AL in MS<sub>2</sub> is demonstrated in Fig.6 (b), when the AL is added, the lowest point of  $Tr=0.66$ , and after adding it consistently maintains a value at  $Tr>0.96$ . Usually, the impedance matching theory is applied to explain the effect of the AL and the equivalent wave impedance of the EM waves can be calculated from the reflection phases computed by the TMM [42]:

$$\frac{Z_{eff}}{Z_0} = Z_{e,eff} + jZ_{i,eff} = \frac{1+r}{1-r}. \quad (33)$$

The wave impedance of EM waves in a vacuum is  $Z_0=377 \Omega$ . Perfect transmission is achieved when the calculated equivalent wave impedance reaches 1 in the real part and 0 in the imaginary part. As shown in Figs.6 (a) and (c), MS<sub>1</sub> the real part of the equivalent impedance between  $35^\circ-60^\circ$  is nearly 1 and the imaginary part is nearly 0. For MS<sub>2</sub>, the impedance matching condition is also satisfied in the range of  $30^\circ-60^\circ$ , as shown in Fig.6 (d). The designed AL effectively performs impedance matching and realizes the anti-reflective effect.



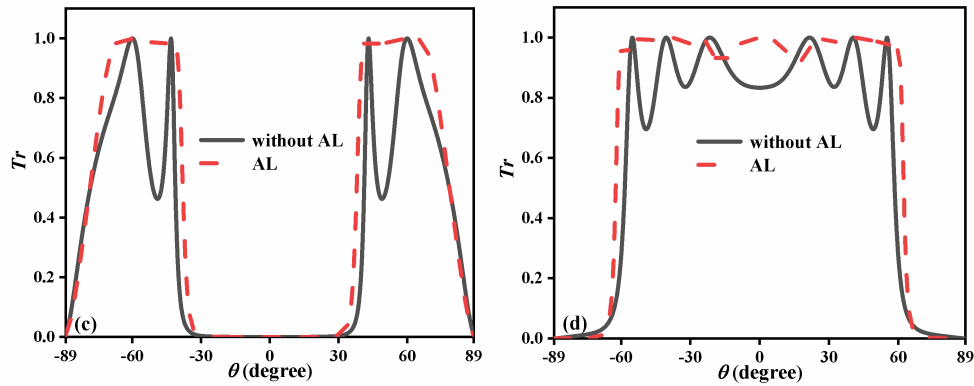
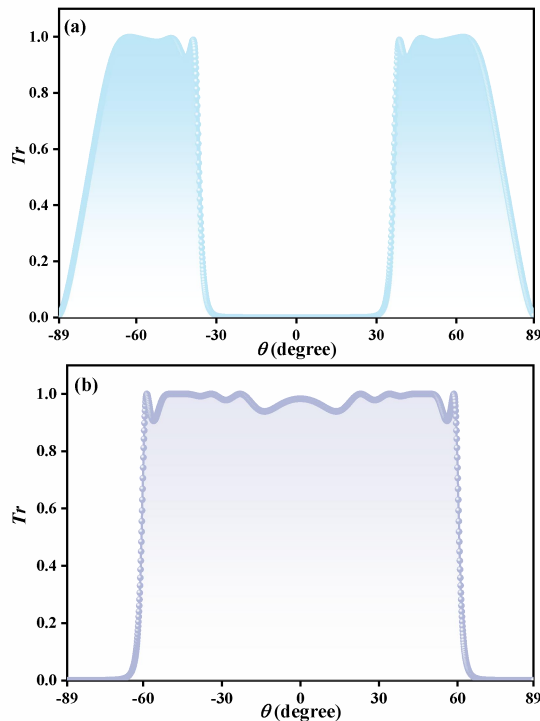


Fig.6. (a) Impedance matching characteristics of MS<sub>1</sub>, (b) Impedance matching characteristics of MS<sub>2</sub>, (c) The effect of the presence or absence of AL on the angle selection function in MS<sub>1</sub>, and (d) in MS<sub>2</sub>.

In Fig.7, when the characteristic of the PBG in Fig.5 in the frequency domain is converted to the angular domain, the effect of angle selection is created. Since the angle edge states in this paper are excited by each isotropic dielectric, they exhibit the same properties at  $+\theta_s$  and  $-\theta_s$ . The angle-selective effect at the left edge is illustrated in Fig.7 (a), where an angle window of high transmission stability is formed at about  $35^\circ$ . In Fig.7 (b), the angle selection of the right edge has excellent properties similar to those of the left edge. When the EM waves penetrate MS<sub>2</sub>, the directional control effect of MS<sub>2</sub> on the EM waves still exists, as shown in Fig.7 (c). Inevitably, when units I and II are spliced together, there is a slight decrease in transmission due to film resonance. However, when the transmission of a single structure is high enough, the high transmission stability of the angle edge state remains when the film resonance occurs.



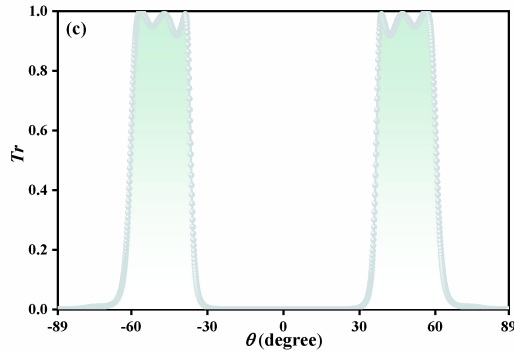


Fig.7. (a) Angle edge state for the left edge of the PBG formation of MS<sub>1</sub>, (b) Angle edge state for the right edge of the PBG formation of MS<sub>2</sub>, and (c) when MS<sub>1</sub> and MS<sub>2</sub> are spliced together.

In this part, MS<sub>1</sub>, MS<sub>2</sub>, and the HMMS are all spliced together, as shown in Fig.1 (d). The PBG consists of each isotropic dielectric that exhibits the same properties on positive and negative scales. The HMMS exhibits selective absorption at  $+\theta_s$  and selective transmission at  $-\theta_s$ . When the three units are spliced, the EM waves first pass through MS<sub>1</sub> and MS<sub>2</sub>, and only the EM waves within the selected angle edge state will be transmitted out of MS<sub>1</sub> and MS<sub>2</sub>, while the EM waves in the rest of the directions will be completely reflected. The angle selection of the HMMS itself is mediocre, and when the EM waves are already selected in the angular domain, the HMMS will only absorb the EM waves transmitted in this case. The angular domain absorption spectrum after splicing is shown in Fig.8 (a). In the  $+\theta_s$ , from 35° to 55°,  $A > 0.9$ , and in the  $-\theta_s$ ,  $A$  is continuously less than 0.1. The present ADTD shows excellent selectivity in the angular domain and achieves the effect of directional absorption, which is of great value in the fields of antenna design, radar protection, wireless transmission, and so on. Noteworthy, the transmission characteristics of this structure are demonstrated in Fig.8 (b), which is opposite to the angle of absorption, maintaining  $Tr > 0.9$  from 35°-50° within the  $-\theta_s$ , and the transmission tends to be close to 0 in the positive angle range. The positive and negative directional absorption and transmission characteristics provide a novel solution for the design of multifunctional devices in the antenna field.

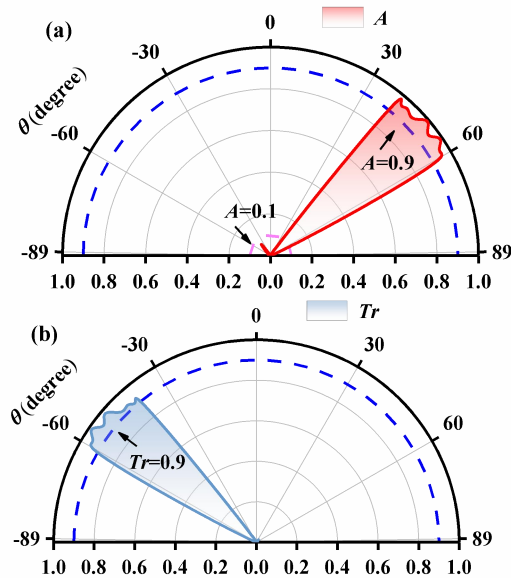


Fig.8. (a) Directional absorption properties of ADTD, and (b) directional transmission properties of ADTD.

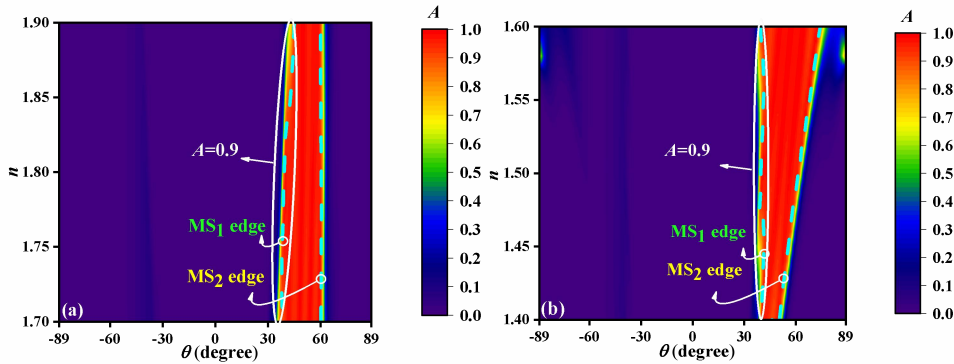


Fig. 9. Variation of dielectric refractive index in ADTD on absorption characteristics, (a)  $n_B$ , and (b)  $n_D$ .

When the dielectric constant of the media in an MS unit changes, the position of the PBG shifts with it, resulting in a movement in the angle edge state. In the given ADTD, there are two angle edge states excited by the PBG. Changing the refractive indexes of the dielectrics in MS<sub>1</sub> and MS<sub>2</sub>, respectively, can move the left and right angle edge states (see Fig.9), respectively. This modulation by refractive index demonstrates the potential angular tunable effect of directionally selective properties. The modulation effect of refractive index change on the angle edge state is illustrated here only theoretically, and adjustment materials can be invoked to achieve the effect in practical design. Low refractive index media in MS structures are used for this section. The effect of the refractive index change of dielectric B in MS<sub>1</sub> is demonstrated in Fig.9 (a), and the dotted line indicates the position of  $A=0.9$ . It follows that when the refractive index becomes larger, the left edge shifts to the right and maintains a better absorption effect. In Fig.9 (b), when the dielectric constant of medium D in MS<sub>2</sub> is changed, the right edge undergoes a corresponding shift to maintain a more stable directional absorption in the range of 1.5-1.6. When both edges are adjusted separately, the other edge remains essentially by itself. This modulation effect for the edges can be realized by introducing a refractive index adjustable medium such as germanium antimony telluride [43], which is only theoretically analyzed here.

The overall thickness  $W$  and the inclination angle  $\varphi$  of the HMMS are two important indicators of the HMMS. In Fig.10 (a) the effect of  $W$  variation on directional absorption is illustrated, with the green line indicating the case of  $A=0.9$ . It is seen that  $W$  has a great effect on the directional absorption when  $W < 1.1$  mm, and  $W$  does not have a great effect on the directional absorption when  $W > 1.1$  mm. As  $W$  tends to a larger value, the ultra-wideband property is excited, and then this is not the focus of this paper and will not be discussed further. In Fig.10 (b), the effect of tilt angle on directional absorption is discussed. The blue dashed line indicates the case of  $A=0.9$ . The performance of the directional absorption changes drastically when  $\varphi$  is varied. The effect of directional selection achieved is to select intervals  $A > 0.9$  in positive angles, and  $A$  is always less than 0.1 in negative angles. To achieve this,  $\varphi$  must be inside the line enclosure of Fig.10 (b). The discussion of  $W$  and  $\varphi$  is potentially valuable for the sizing and layout design of the HMMS.

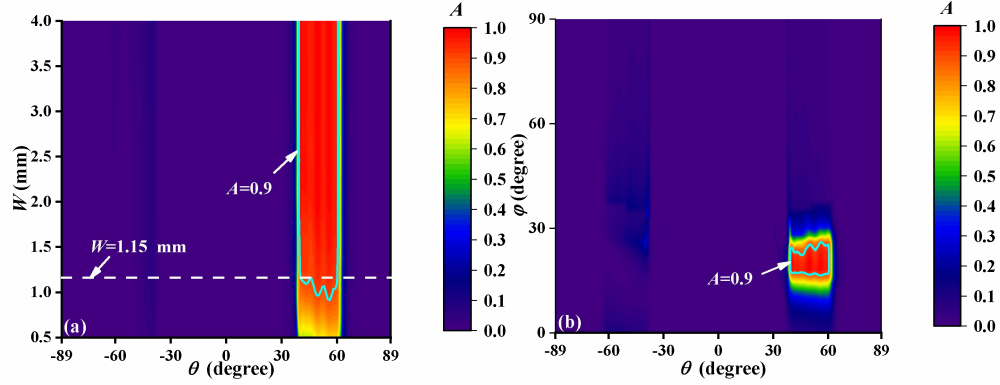


Fig.10. (a) Absorptivity of HMMS as functions of the  $\theta$  and  $W$  of HMMS, the solid line indicates the case where  $A=0.9$ , and (b)  $A$  as functions of the  $\theta$  and  $\varphi$  of HMMS.

In this paper, the TMM is used to numerically calculate the results. In the study of optical thin films, TMM has been widely used and proven to be consistent with practical results. However, there has been no experimental verification of the equivalent calculation method for HMMS. Due to the unique properties of solid-state plasma, there is currently no precise process for its preparation, making it difficult to experimentally verify the design presented in this article. To make the results more convincing, we used the Finite Element Method (FEM) method to validate the results. The absorption curve in the frequency domain at  $\theta=56.7^\circ$  is plotted in Fig.11. Among them, Fig.11 (a) is the result obtained by calculating using the transition matrix method derived in the article. The results obtained using FEM are shown in Fig.11 (b). It can be seen that the difference between the two algorithms is mainly around  $f_1=22$  GHz. The results obtained by TMM have an absorption jump, while the results obtained by FEM do not. The reason is that when using TMM,  $k_z^1$  and  $k_z^2$  represent two wave vectors with opposite directions of travel, but the imaginary parts of  $k_z^1$  and  $k_z^2$  will cross the coordinate axis near  $f_1$ . In TMM, the sign of the imaginary part of the wave vector represents the gain and loss of the wave. To keep the loss properties unchanged, improvement processing was performed when the imaginary parts of  $k_z^1$  and  $k_z^2$  jumped. This processing method causes a sudden change in the value of the imaginary part, resulting in discontinuous values near  $f_1$  and exhibiting a jumping phenomenon in the frequency domain. The frequency point studied in this article is at  $f=19.5$  GHz, and the difference at  $f_1$  does not affect the final results.

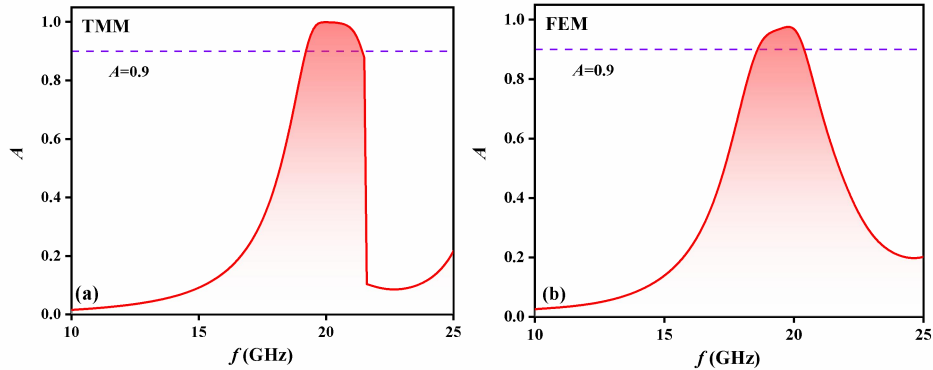


Fig.11. Absorption spectra of HMMS obtained by different methods; (a) TMM, and (b) FEM.

The numerical calculation methods for thin film optics are already very mature, among which TMM is a widely recognized method. There are two forms of TMM, one is the generalized TMM, which is the phase matrix, and the other is calculated layer by layer, which is the characteristic matrix method [29]. Figs.12 (a) and (b) respectively show the numerical

results of two forms of TMMs, and the lines are basically consistent. There is a slight difference in the frequency position where PBG is located, which is due to different processing methods used to describe the phase and magnitude changes of the EM field. The calculation results of FEM are shown in Fig.12 (c), with almost no difference from the results in Figs.12 (a) and (b). The reliability of the calculation results of the proven PBG.

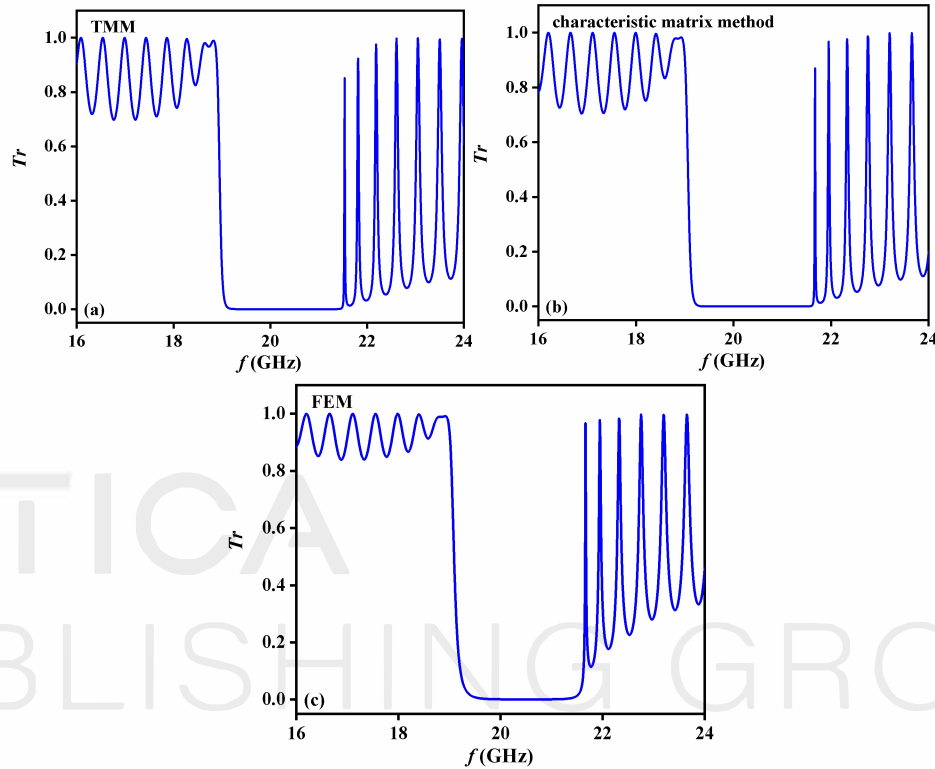


Fig.12. Transmission spectral lines of PBG obtained by different methods (a) TMM, (b) characteristic matrix method, and (c) FEM.

In actual applications, changes in material properties may cause a shift in the frequency of the highest transmission-absorption point of HMMS. For this situation, the thickness of MS can be adjusted to match the new frequency point. In the characteristic matrix method, the variable that changes with frequency is the phase of a single-layer optical film. As long as the phase term remains unchanged numerically, the original angle selection effect can be maintained. In the design, it is only necessary to keep the product of the thickness and frequency of this optical thin film constant. The specific calculation formula of the TMM can refer to Ref. [29], no further elaboration will be made here. Through the dynamic design of MS and the phenomenon excitation of HMMS, similar effects can be achieved in any optical band, which has high theoretical value and reliability.

Table 1. The performance comparison.

Refs.	Configuration	Wave band	Asymmetric	Theory	Selectivity
[27]	One-dimensional films	Medium-infrared	No	Gradient ENZ	$A > 0.6$ & $A < 0.2$
[28]	Photonic crystals	Near-infrared	No	Embedded eigenstates and quasi-embedded eigenstates	$A > 0.7$ & $A < 0.1$
[44]	Unperturbed metasurface	Medium-infrared	Yes	Asymmetric directional control	$A > 0.6$ & $A < 0.3$
[45]	Smooth grating	Near-infrared	No	Coherent spontaneous emission	$A > 0.6$ & $A < 0.1$
[46]	Polar material	Near-infrared	No	Wolf effect	$A > 0.9$ & $A < 0.2$
This work	MS+HMMS	Microwave	Yes	Asymmetric transmission-absorption+PBG	$A > 0.9$ & $A < 0.1$

To systematically visualize the superior performance of the proposed ADTD, Table 1 is plotted, where the “selectivity” column indicates the value of  $A$  in selected and unselected regions. Table 1 lists five devices with directional selection functions implemented by different means. Through these comparisons, it is easy to realize that the selectivity of ADTD achieves unique results. Moreover, the presented ADTD can be adjusted in thickness and material according to the desired operating band. Ultra-wideband, tunable functions can be achieved through the rational design of several parameters of the ADTD.

#### 4. Conclusion

In summary, an ADTD is presented. Excellent asymmetric selectivity is achieved by combining multiple angle selection principles. The limitations of conventional angle selection, which is only capable of achieving the same function in  $+\theta_s$  and  $-\theta_s$  are overcome. The design has potential applications in surface protection, and optical encryption, providing advanced theoretical contributions for optical surface design. Furthermore, the dynamic regulation of transmission-absorption windows and ultra-wideband absorption can be achieved based on this design by the technical means mentioned. This scheme is of great significance for the construction of optical materials and the design of multifunctional optical devices.

**Funding.** This work is supported by the National Key Research and Development Program of China (No.2022YFA1405000), the National Natural Science Foundation of China (No. 62375141), the Natural Science Foundation of Jiangsu Province, Major Project (No. BK20212004), and the National College Students Innovation and Entrepreneurship Training Program (Grant No. 202410293019Z).

**Disclosures.** The authors declare no conflicts of interest.

**Data availability.** Data underlying the results presented in this paper are not publicly available at this time but may be obtained from the authors upon reasonable request.

#### References

1. Y. Liu, Y. Liu, and M. G. B. Drew, "A Re-evaluation of the mechanism of microwave absorption in film - Part 2: The real mechanism," *Materials Chemistry and Physics* 291, 126601 - 126601 (2022).
2. Y. Xia, W. Gao, and C. Gao, "A Review on Graphene - Based Electromagnetic Functional Materials: Electromagnetic Wave Shielding and Absorption," *Advanced Functional Materials* 32(42), 2204591 - 2204591 (2022).
3. Viktor Asadchy, Ihar Faniayeu, Younes Ra'di, Sergei Khakhomov, Igor Semchenko, and S. A. Tretyakov, "Broadband Reflectionless Metasheets: Frequency-Selective Transmission and Perfect Absorption," *Physical Review X* 5(3), (2015).

4. D. Schurig, J. J. Mock, B. J. Justice, S. A. Cummer, J. B. Pendry, A. F. Starr, and D. R. Smith, "Metamaterial Electromagnetic Cloak at Microwave Frequencies," *Science* 314(5801), 977 – 980 (2006).
5. I. Choi, D. Lee, and D. G. Lee, "Optimum design method of a nano-composite radar absorbing structure considering dielectric properties in the X-band frequency range," *Composite Structures* 119, 218 – 226 (2015).
6. V. G. Veselago, "The Electrodynamics of Substances with Simultaneously Negative Values of  $\epsilon$  and  $\mu$ ," *Soviet Physics Uspekhi* 10(4), 509 – 514 (1968).
7. J. B. Pendry, A. J. Holden, D. J. Robbins, and W. J. Stewart, "Magnetism from conductors and enhanced nonlinear phenomena," *IEEE Transactions on Microwave Theory and Techniques* 47(11), 2075 – 2084 (1999).
8. K. L. Smith and R. S. Adams, "Spherical Spiral Metamaterial Unit Cell for Negative Permeability and Negative Permittivity," *IEEE Transactions on Antennas and Propagation* 66(11), 6425 – 6428 (2018).
9. D. R. Smith, D. Schurig, and J. J. Mock, "Characterization of a planar artificial magnetic metamaterial surface," *Physical Review E* 74(3), (2006).
10. J. Hao, Q. Ren, Z. An, X. Huang, Z. Chen, M. Qiu, and L. Zhou, "Optical metamaterial for polarization control," *Physical Review A* 80(2), (2009).
11. N. I. Landy, S. Sajuyigbe, J. J. Mock, D. R. Smith, and W. J. Padilla, "Perfect Metamaterial Absorber," *Physical Review Letters* 100(20), (2008).
12. N. B.-X. Wang, N. G.-Z. Wang, N. L.-L. Wang, and N. X. Zhai, "Design of a Five-Band Terahertz Absorber Based on Three Nested Split-Ring Resonators," *IEEE Photonics Technology Letters* 28(3), 307 – 310 (2015).
13. W. Huang, S.-T. Cao, X. Qu, W. Zhang, S. Yin, and J. Han, "Inverse Design of Metamaterial Bound States in the Continuum Device via Coupled Mode Theory," *IEEE Transactions on Microwave Theory and Techniques* 72(3), 1520 – 1528 (2024).
14. Y. J. Kim, Y. J. Yoo, K. W. Kim, J. Y. Rhee, Y. H. Kim, and Y. Lee, "Dual broadband metamaterial absorber," *Optics Express* 23(4), 3861 (2015).
15. F. Costa, A. Monorchio, and G. Manara, "Analysis and Design of Ultra Thin Electromagnetic Absorbers Comprising Resistively Loaded High Impedance Surfaces," *IEEE Transactions on Antennas and Propagation* 58(5), 1551 – 1558 (2010).
16. M. Entezari and M. Zavvari, "Application of Hyperbolic Metamaterials for Responsivity Enhancement of Thin Film Photo-Conductive Detectors," *IEEE Sensors Journal* 16(24), 8916 – 8920 (2016).
17. E. E. Narimanov, "Photonic Hypercrystals," *Physical Review X* 4(4), (2014).
18. A. A. High, R. C. Devlin, A. Dibos, M. Polking, D. S. Wild, J. Perczel, N. P. de Leon, M. D. Lukin, and H. Park, "Visible-frequency hyperbolic metasurface," *Nature* 522(7555), 192 – 196 (2015).
19. E. Yablonovitch, "Inhibited Spontaneous Emission in Solid-State Physics and Electronics," *Physical Review Letters* 58(20), 2059 – 2062 (1987).
20. Y. Wang, D. Cui, Y. Wang, G. Yang, and C. Wang, "Electrically and thermally tunable multifunctional terahertz metasurface array," *Physical review A* 105(3), (2022).
21. Z. Yu, C. Hou, Y. Yuan, P. Xu, X. Dong, J. Yang, L. Yuan, Y. Wang, and Y. Qin, "High Accuracy Distributed Polarization Extinction Ratio Measurement For a Polarization-Maintaining Device With Strong Polarization Crosstalk," *Journal of Lightwave Technology* 39(7), 2177 – 2186 (2020).
22. K. Yin, Y. Qu, S. E. Kooi, W. Li, J. Feng, Jo Ann Ratto, J. D. Joannopoulos, M. Soljačić, and Y. Shen, "Enabling Manufacturable Optical Broadband Angular-Range Selective Films," *ACS Nano* 15(12), 19917 – 19923 (2021).
23. C. Bian, Y. Zhong, X. Chen, T. Low, H. Chen, B. Zhang, and X. Lin, "Janus faces of dipolar sources in directional near-field coupling with an oriented misalignment," *Physical review A* 109(3), (2024).
24. Y. Shen, D. Ye, I. Čelanović, S. G. Johnson, J. D. Joannopoulos, and M. Soljačić, "Optical Broadband Angular Selectivity," *Science* 343(6178), 1499 – 1501 (2014).
25. H. Iizuka, N. Engheta, and S. Sugiura, "Extremely small wavevector regime in a one-dimensional photonic crystal heterostructure for angular transmission filtering," *Optics Letters* 41(16), 3829 (2016).
26. Y. Qu, Y. Shen, K. Yin, Y. Yang, Q. Li, M. Qiu, and M. Soljačić, "Polarization-Independent Optical Broadband Angular Selectivity," *ACS photonics* 5(10), 4125 – 4131 (2018).
27. J. Xu, J. Mandal, and A. P. Raman, "Broadband directional control of thermal emission," *Science* 372(6540), 393 – 397 (2021).
28. M. Q. Liu and C. Y. Zhao, "Near-infrared nonreciprocal thermal emitters induced by asymmetric embedded eigenstates," *International Journal of Heat and Mass Transfer* 186, 122435 – 122435 (2022).
29. B.-F. Wan, H.-N. Ye, and H.-F. Zhang, "Multi-channel angular selective window based on the epsilon-near-zero features of  $\text{YBa}_2\text{Cu}_3\text{O}_7$  material and photonic crystals ceramic structure of extremely small dispersion edge regions," *Ceramics International* 49(22), 34814 – 34825 (2023).
30. L. Wu, Y. Jia, L. Jiang, J. Guo, X. Dai, Y. Xiang, and D. Fan, "Sensitivity Improved SPR Biosensor Based on the  $\text{MoS}_2$ /Graphene – Aluminum Hybrid Structure," *Journal of Lightwave Technology* 35(1), 82 – 87 (2017).
31. D. Frese, Q. Wei, Y. Wang, L. Huang, and T. Zentgraf, "Nonreciprocal Asymmetric Polarization Encryption by Layered Plasmonic Metasurfaces," *Nano Letters* 19(6), 3976 – 3980 (2019).
32. L. Fan, J. Wang, L. T. Varghese, H. Shen, B. Niu, Y. Xuan, A. M. Weiner, and M. Qi, "An All-Silicon Passive Optical Diode," *Science* 335(6067), 447 – 450 (2012).

33. E. D. Kosten, J. H. Atwater, J. Parsons, A. Polman, and H. A. Atwater, "Highly efficient GaAs solar cells by limiting light emission angle," *Light: Science & Applications* 2(1), e45 - e45 (2013).
34. Y. Gao, B. Li, R. Wang, Q. Yan, Jiangtao Huangfu, and D. Ye, "Polarization-Independent Broadband Angular Selectivity Based on Anisotropic Diamagnetic Metamaterial," *IEEE transactions on antennas and propagation* 70(8), 7306 - 7310 (2022).
35. I. A. Starkov and A. S. Starkov, "Maxwell - Garnett model for thermoelectric materials," *International Journal of Solids and Structures* 202, 226 - 233 (2020).
36. X.-K. Kong, J.-J. Mo, Z.-Y. Yu, W. Shi, H.-M. Li, and B.-R. Bian, "Reconfigurable designs for electromagnetically induced transparency in solid state plasma metamaterials with multiple transmission windows," *International Journal of Modern Physics B* 30(14), 1650070 - 1650070 (2016).
37. Y. Fang and Y. Zhang, "Perfect Nonreciprocal Absorption Based on Metamaterial Slab," *Plasmonics* 13(2), 661 - 667 (2017).
38. Igor Bando, K. Lechner, D. Sorokin, and P. K. Townsend, "Nonlinear duality-invariant conformal extension of Maxwell's equations," *Physical review D* 102(12), (2020).
39. S. V. Zhukovsky, Andrei Andryeuskii, J. E. Sipe, and A. V. Lavrinenko, "From surface to volume plasmons in hyperbolic metamaterials: General existence conditions for bulk high-k waves in metal-dielectric and graphene-dielectric multilayers," *Physical Review B* 90(15), (2014).
40. R. Afzalzadeh, "Dielectric constant measurements of finite-size sheet at microwave frequencies by pseudo-Brewster's angle method," *IEEE Transactions on Microwave Theory and Techniques* 46(9), 1307 - 1309 (1998).
41. C. Du, D. Zhou, H. Guo, Y. Pang, H. Shi, W. Liu, J. Su, C. Singh, S. V. Trukhanov, L.V. Panina, and Z. Xu, "An ultra-broadband terahertz metamaterial coherent absorber using multilayer electric ring resonator structures based on anti-reflection coating," *Nanoscale* 12(17), 9769 - 9775 (2020).
42. T.-W. Chang, C.-H. Huang, D. J. Hou, C.-J. Wu, and D.-X. Chen, "Analysis of Unidirectional Absorption in a Defective Superconducting Photonic Crystal," *IEEE photonics journal* 9(4), 1 - 9 (2017).
43. A. Tittl, A.-K. U. Michel, M. Schäferling, X. Yin, B. Gholipour, L. Cui, M. Wuttig, T. Taubner, F. Neubrech, and H. Giessen, "Plasmonic Absorbers: A Switchable Mid-Infrared Plasmonic Perfect Absorber with Multispectral Thermal Imaging Capability," *Advanced Materials* 27(31), 4526 - 4526 (2015).
44. J. Yu, R. Qin, Y. Ying, M. Qiu, and Q. Li, "Asymmetric Directional Control of Thermal Emission," *Advanced Materials* 35(45), (2023).
45. F. Marquier, K. Joulain, J.-P. Mulet, R. Carminati, J.-J. Greffet, and Y. Chen, "Coherent spontaneous emission of light by thermal sources," *Physical Review B* 69(15), (2004).
46. J.-J. Greffet, R. Carminati, K. Joulain, J.-P. Mulet, S. Mainguy, and Y. Chen, "Coherent emission of light by thermal sources," *Nature* 416(6876), 61 - 64 (2002).